UNIVERSITÀ DEGLI STUDI DEL SANNIO

DIPARTIMENTO DI INGEGNERIA
Settore scientifico disciplinare ING-INF/02

Progetto

"Advanced VIRGO PLUS Coating Research & Development"
finanziato da EGO (European Gravitatonal Observatory)

Relazione delle Attività

DEPOSIZIONE E CARATTERIZZAZIONE
DI FILM COMPOSITI NANOSTRATIFICATI
BASATI SU OSSIDI VETROSI

Responsabile Scientifico
Prof. Vincenzo Pierro

Titolare del Contratto
Ph.D. Roberta De Simone

Scientific basis: State-of-the-art

The past decade has seen the ramp-up of the second-generation ('Advanced') earth-based gravitational-wave (GW) detectors. Design improvements and technological upgrades have paved the way to the first direct detection of GWs by the global network made up of the two aLIGO instruments [1] (located in the USA: Hanford, WA and Livingston, LA) and of the Advanced Virgo detector [2] (located in Cascina, Italy). The main results achieved by the LIGO Scientific Collaboration and the Virgo Collaboration – recently joined by the KAGRA Collaboration (located in Kamioka, Japan, under the Ikenoue mountain) – include the first detection of a binary black hole merger (GW150914 [3]); the first detection of a binary neutron star (BNS) merger (GW170817 [4]) that lead to the birth of multi-messenger astronomy with GW [5]; and now dozens of detections of compact binary mergers that add up in a GW Transient Catalogue regularly updated [6]- [7]. These detections contribute to opening a new window onto the Universe by providing insights to the populations of compact objects and the binary merger rates [8]; they also allow scientists to perform stringent tests of general relativity [9] in a new regime of gravitation never probed before. Advanced Virgo is a power-recycled Michelson interferometer with Fabry-Perot cavities in its 3 km-long arms. By measuring interferometric figure due to the length differences between mirrors in the arms interferometer, gravitational waves are identified. Therefore, very sensitive interferometers that accurately measure the separation between suspended test masses coated to works as highly reflecting mirrors have been designed in order to detect gravitational waves. A core challenge is the optimization of the mirrors for GW detectors. It is important to discover a mirror configuration that produces the least amount of additional (thermal) noise on the detection channel in addition to the typical mirror optimization design request of achieving high reflectance in a given frequency and angular range. It is well known that high reflectance, low absorption, mirrors typically consist of multilayers of alternating low and high refractive index materials, L and H respectively, where each layer is quarter wave thick at the operating frequency. As a result, a simple formulation of the coating optimization problem for the design of low noise dielectric mirrors can involve looking for the sequence of thicknesses of the selected materials

that make up the mirrors that minimizes the thermal noise while maintaining the transmittance below a specified threshold value.

Research activities

The (dielectric-multilayer based) cavity mirror (test-mass) reflective coatings currently used in the dielectric mirrors of both Virgo and LIGO [10] [11] are based on two materials developed mainly by the Laboratoire des Matériaux Avancés (LMA) [12], namely Titania-doped Tantala (TiO_2:: Ta_2O_5) and silica (SiO_2).
To improve the multilayers structures performance, it has been formulated and solved another design that consist in discovering (synthesizing and optimizing) improved materials that have increased optical contrast, fewer optical and mechanical losses and enabling the achievement of a specified transmittance with fewer layers, resulting into thinner coatings and lower noise and giving up the constraint of having only two constituent materials and, then, introducing new ternary multimaterial design. A check of the robustness against the inaccuracy of the deposition process has been also carried out. Furthermore, none of the materials present in nature and studied at this time qualifies as a straight substitute for the materials currently in use with the highest optical losses (TiO_2-doped Ta_2O_5 in current setups), but a few of them are better in terms of some properties (e.g., optical density, and/or mechanical losses), while unfortunately worse regarding others. The optimal material can be synthesized by using *Nanolayered structure* (NL) with thickness and equivalent refractive index that must be chosen ad hoc to fulfill the imposed conditions: at this scope it has been introduced a novelty homogenization procedure based on an established technique, the *Abelès method*.

Background of our Research Group

The Uni Sannio/Salerno group has been active in both research directions [13]: i) the search of new material, and ii) the optimization of coating design using the available ones. As regards coating design optimization, our ET/Virgo working group originated the design of the aLIGO-AdVirgo mirrors presently in use [14]-[15], and recently extended the same design philosophy (layer thickness optimization for thermal noise minimization under prescribed transmittance and absorbance upper bounds) also to coatings using three different

materials rather than two, the third material being amorphous Silicon (a-Si), Silicon Nitride ($SiNx$) or Germanium Oxide (GeO_2) - these could not be used in a binary design due to their relatively large optical losses, but offer large dielectric contrast and lower mechanical losses at cryogenic temperatures compared to those presently in use. Our group, also introduced the idea, in collaboration with the NTHU group led by Prof. Chao Shiuh [16], of producing high-index films, of the needed optical thickness (typically, one quarter of the local wavelength) using nm-scale plane-layered composites consisting of alternating nanolayers of different materials. Nanolayering has been shown to yield two potential benefits. It hinders the onset of crystallization during the post-deposition annealing treatment needed to stabilize the film, hence hindering also the related blow-up of optical scattering and mechanical dissipation. It also shifts/reshapes the mechanical loss-peak observed in these materials at cryo temperatures, which is important to tame in view of cryogenic 3G detectors [16]. The nanofilm deposition technology is relatively well established, being widely used to produce X-ray mirrors [17], and filters [18].

Description of the present Work

The research activity done in this project has been focused on i) optimizing the deposition of nanolayered films using the ion-assisted e-beam deposition facility owned by our Virgo/ET working Group at UniSannio, ii) characterizing the film morphology and structure using the AFM, XRD, RS and STEM facilities owned by our Virgo/ET working Group at UniSa and last iii) designing and characterizing optimal nanostratified structures with special attention to the measurement of optical parameters. Several material combinations have been investigated, from a pool including SiO_2, TiO_2, ZrO_2, Al_2O_3, Ta_2O_5, Nb_2O_5. The results have been reported in a number of documents already uploaded on the Virgo-TDS and LIGO-DCC. The present document focuses on two candidate nanolayered composites: Silica/Titania and Silica-Alumina, credited as the most promising substitutes, in the class of nanolayered composites, for the L and H materials currently in use [19] [20].

Deposition facility characterization and upgrade

All films were deposited using the UniSannio owned OptoTech OAC-75RF coater. In its original configuration (Figure 1), the coater features an electron

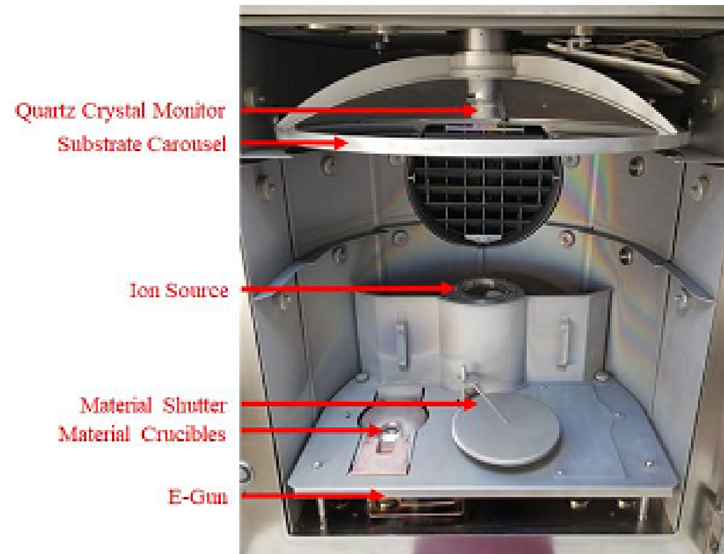

Figure 1: Initial (original) configuration of the OptoTech OAC-75RF coater

gun for material evaporation and, a plasma source for ion assisted deposition. Unlike ion-beam sputterer-based coatings, where metals are projected towards the substrate and oxidized in-flight or after landing, e-beam based coaters evaporate directly the oxide contained in a crucible. Evaporation may produce comparatively less dense films; to prevent this, ion bombardment from a plasma source is used to compactify the ad-atoms by continuously "re-melting" them at the atomic scale. The factory recommended gas mixture used for the plasma is typically 20 sccm O_2 (needed to ensure adequate stoichiometry of the deposited oxides) and 5 sccm Ar. A carousel carrying the substrates rotates above the evaporation plumes so that the ion source can make its work every time the evaporation adds one to a few new atomic layers. A shutter between the evaporation source and the substrates starts and stops the deposition of material onto the substrates, being actuated by the coater digital control unit, on the basis of the continuously monitored film thickness. This latter is measured using a set of quartz-crystals positioned in the center of the chamber at the same approximate height as the substrates, using a calibrated model relating their resonant frequency to the thickness of the deposited material.

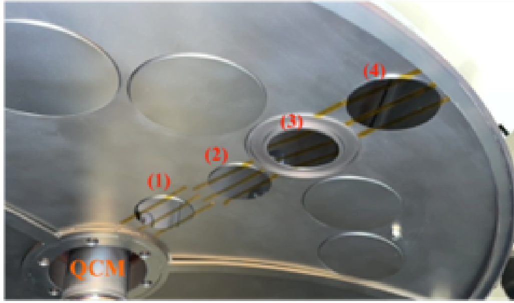

Figure 2: 2-inch substrates mounted along the diameter of the carousel for thickness uniformity assessment. QCM, Quartz Crystal Monitor.

Film thickness homogeneity assessment

Thickness homogeneity of the various deposited films was assessed. Here we report the results for a (nominally $1\mu m$ thick) films of Ta_2O_5 deposited with a rate of $1\AA$/s on a batch of 2 inch diameter circular substrates arranged along the diameter of the carousel at various distances from the carousel center (where the quartz crystal monitors are located), as shown in Figure 2. The thicknesses of the deposited films was measured using a KLA Alpha-Step D500 stylus profilometer (Figure 3a). For each film-coated disk, 5

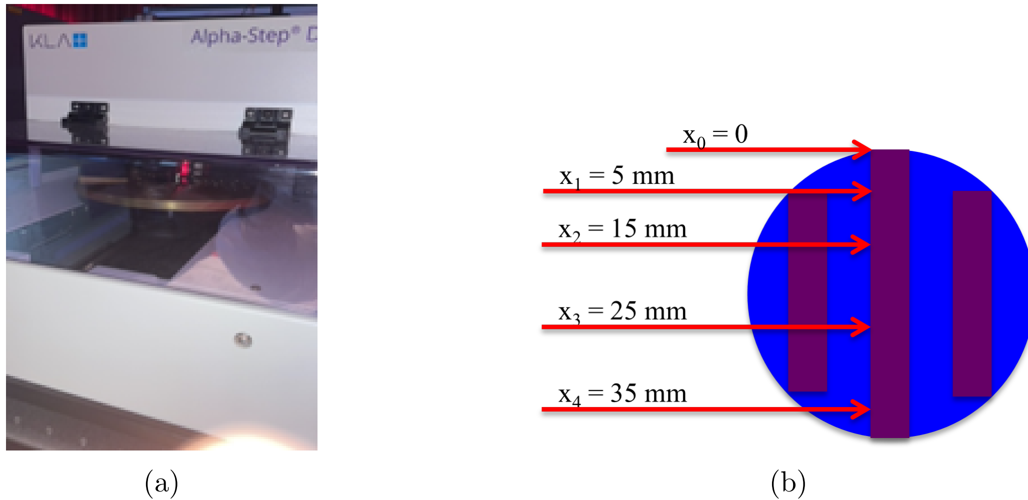

Figure 3: (a) The KLA Alpha-Step D500 stylus profilometer. (b) Thickness measurement points for each sample.

thickness measurements were acquired at different distances from the disk rim, as sketched in Figure 3b.
The results are summarized in Figures 4(a)-(d).

The measured values are well fitted using the function:

$$f(x) = m_1 + \frac{m_1}{\pi} \cdot \arctan\left((x - m_3) \cdot m_4\right) + m_5 \cdot x \tag{1}$$

All film thickness measurements are gathered in Table 1 and Figure 5. Two red lines are guides to eye. In the graph shown in Figure 5, some data is out of range. Not unexpectedly, the deposition thickness is not uniform vs the radial position of the substrates on the carousel. However, there's clearly a "sweet zone", roughly 30 cm in diameter, where the deposition is fairly uniform; and the measured thickness decays almost linearly with radial distance thereof. A further improvement in thickness uniformity may be obtained inserting suitable shades to block the less uniform/stable sections of their respective plumes. This work is on-going, at lower priority.

Deposition facility upgrade

A critical step for improving the quality of the films has been the installation of a second electron gun in the chamber. With two guns, the two materials to be deposited in nanolayers can be kept close to their respective evaporating temperatures throughout the deposition. When a layer is ready to be deposited, a small power increase is sufficient to start evaporation and can be followed almost immediately by the opening of the shutter. This greatly stabilizes the coater operation; temperature and pressure fluctuations are much smaller, the crucibles are not subjected to dozens of cycles of melting-and-hardening, and the overall temperature excursion during deposition is reduced. The second e-gun (identical to the first, Ferrotec EV-M6 multi pocket EB-Gun) was installed, as shown in Figure 6.

In addition to a hardware upgrade (addition of a second e-beam gun), software upgrades were also made to solve some problems. Such upgrades have been necessary since the first deposited films were systematically thicker than expected. The underlying issue was a fundamental flaw with the way the layer thicknesses are measured. Quartz crystal monitors (QCM) are the industry standard for evaporation. They are a faster, more convenient, and cheaper alternative to optical or interferometric thickness monitoring. The flaw is that the software was designed to end the deposition of a layer by closing the shutter once the target layer thickness is measured using the QCM,

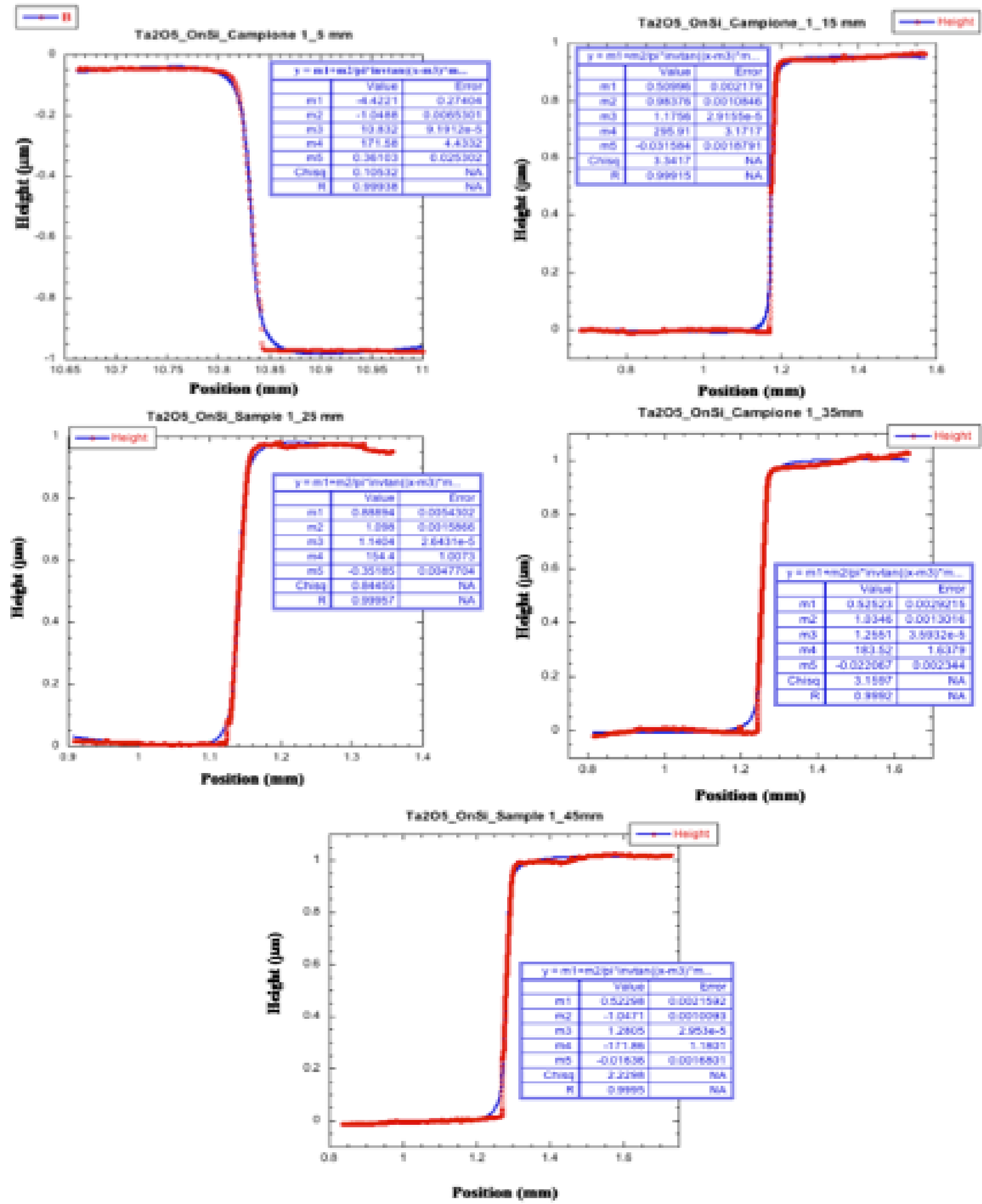

(a)

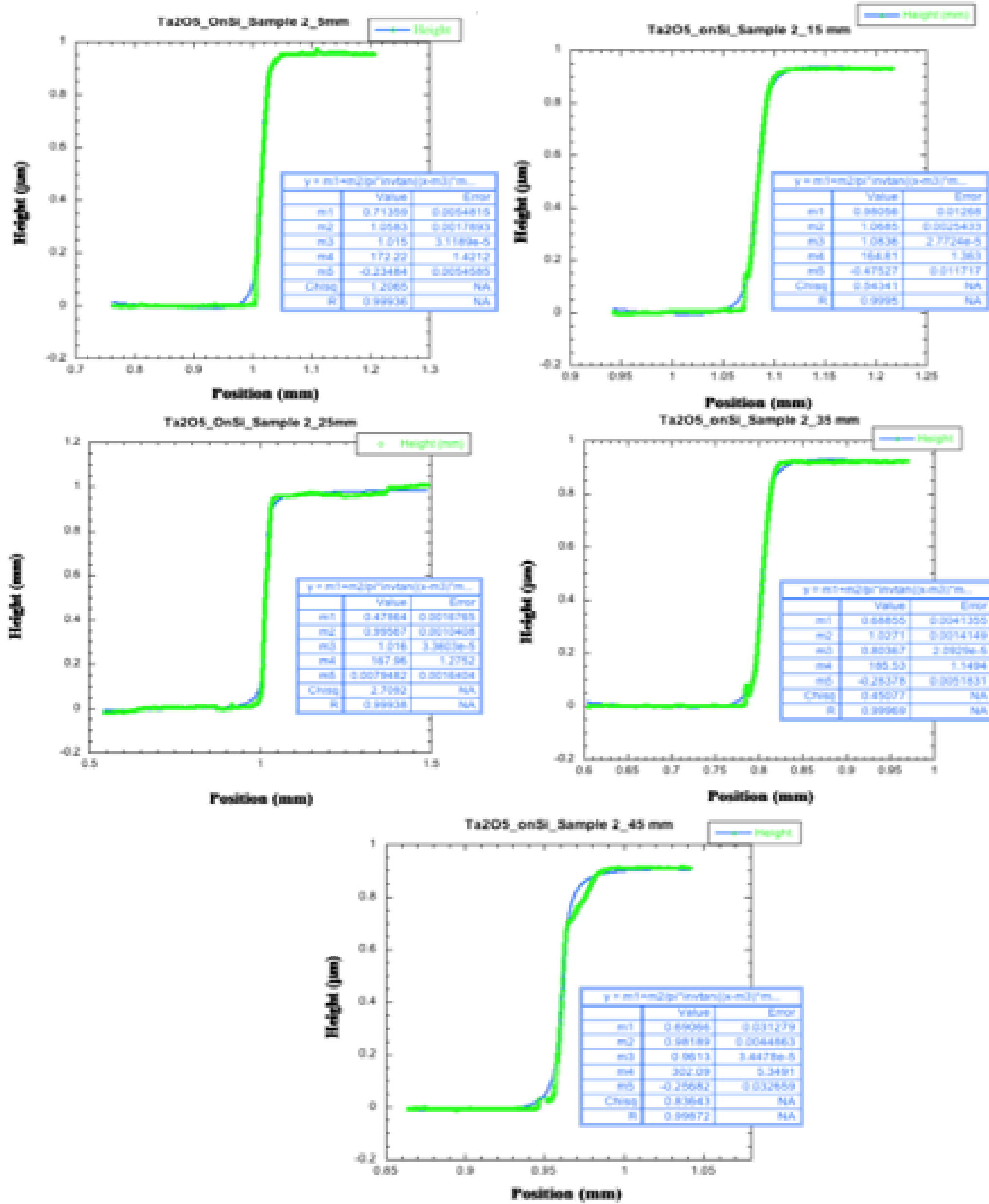

(b)

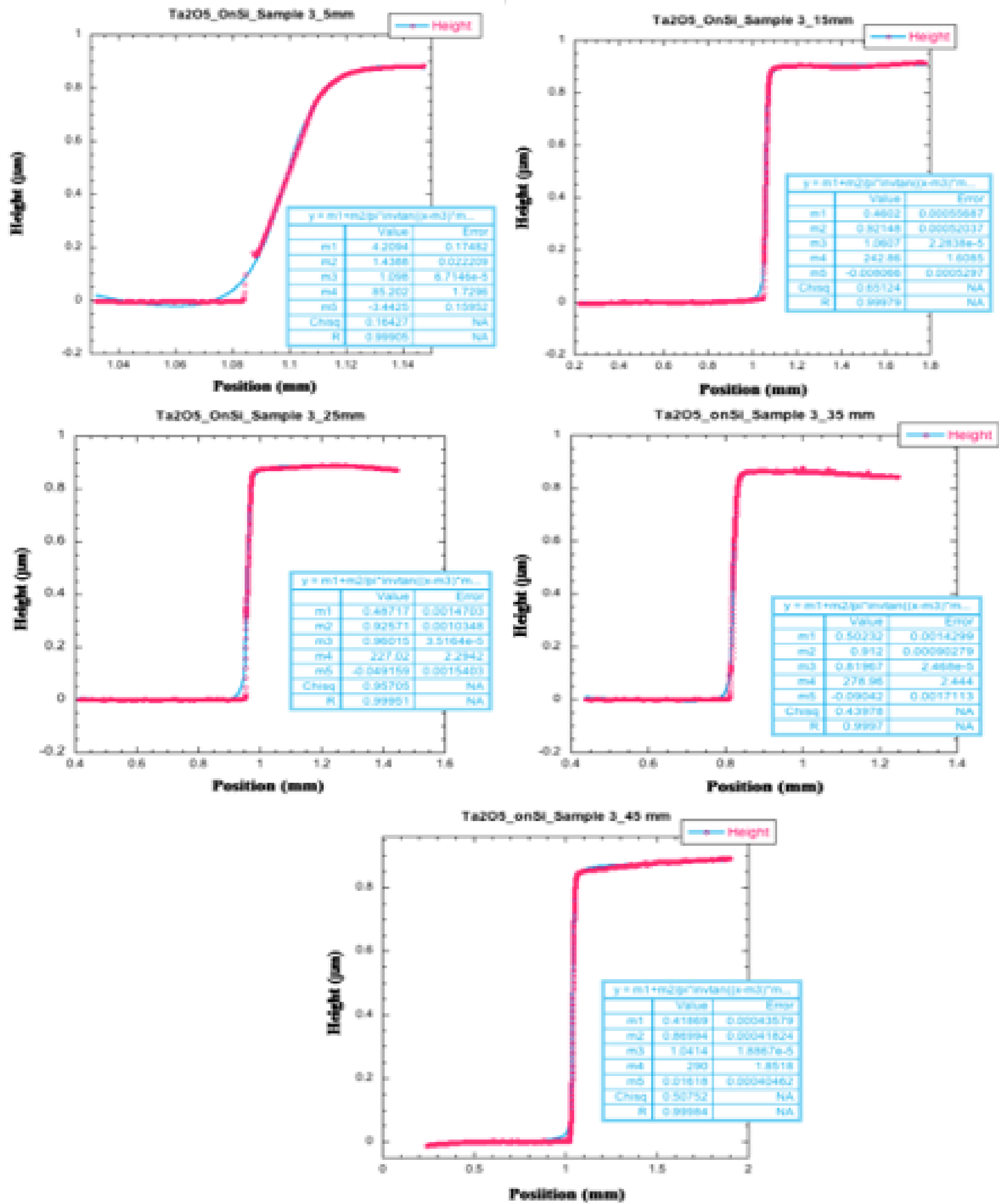

(c)

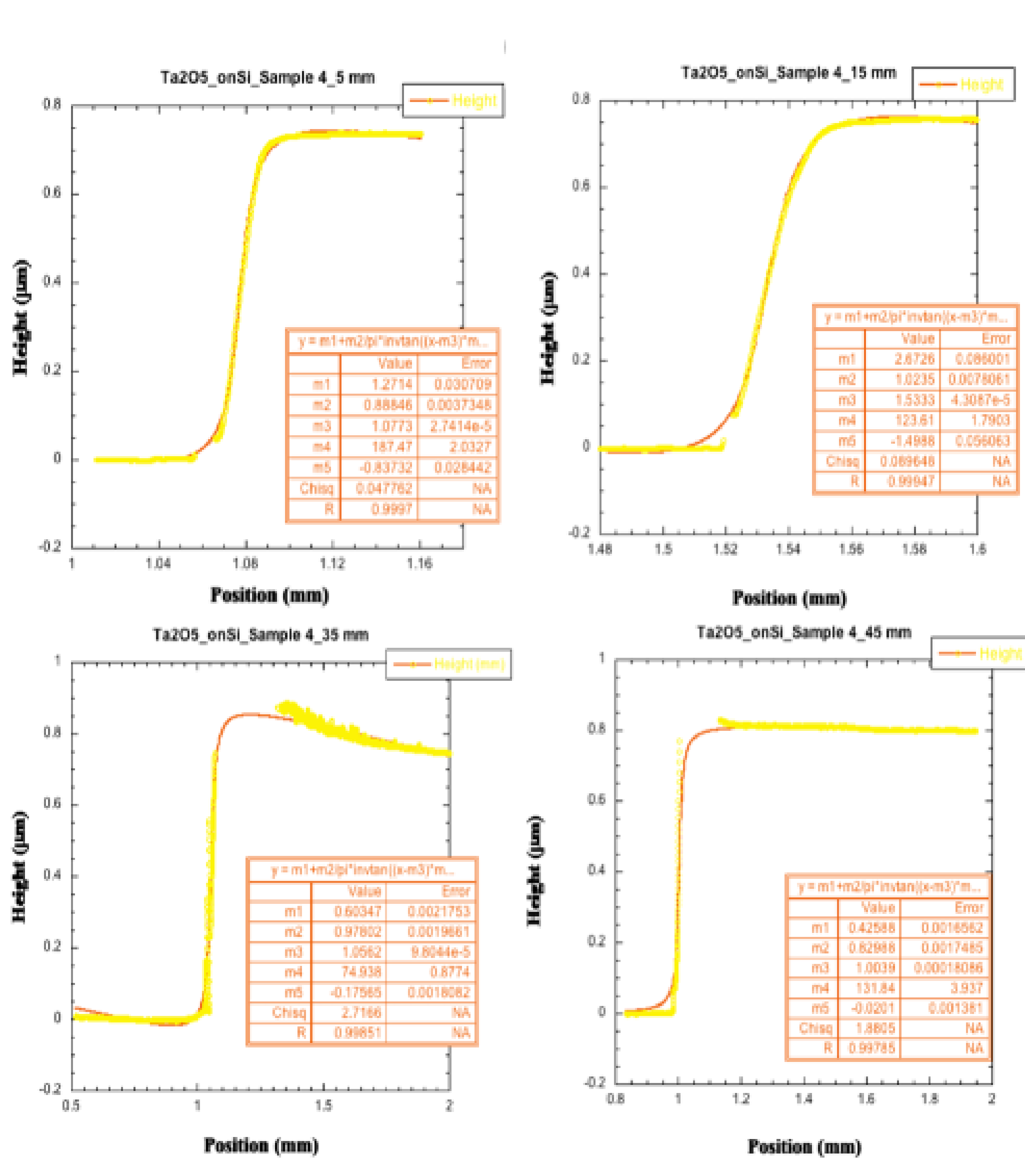

(d)

Figure 4: Measured deposited film thickness (nominal value 1 µm) for samples 1 to 4 in Figure 3 corresponds to plots (a) to (d).

Position (mm)	**Thickness** (mm)
41	1.049 ± 0.006
51	0.984 ± 0.001
61	1.098 ± 0.002
71	1.035 ± 0.001
81	1.047 ± 0.001
116	1.058 ± 0.002
126	1.068 ± 0.002
136	0.996 ± 0.001
146	1.027 ± 0.001
156	0.982 ± 0.004
180	1.44 ± 0.02
190	0.9215 ± 0.0005
200	0.926 ± 0.001
210	0.9120 ± 0.0009
220	0.8699 ± 0.0004
251	0.888 ± 0.004
261	1.0235 ± 0.0008
281	0.978 ± 0.002
291	0.82988 ± 0.002

Table 1: Measurement of the thickness of deposition (nominal $1\mu m$) as function of distance from the center of rotation of the carousel.

but this method has some problems. The main problem is known as QCM thermal shock. When the shutter first opens, the hot material flow suddenly changes the temperature of the quartz, shifting its frequency and giving the illusion of a negative deposition rate. At the end of the layer, when the hot flow is cut off, the cooling mimics a higher deposition rate. This effect is transient and different for each material being evaporated. The first approach to solving this problem was to modify the settings in the existing software to counteract the thermal shock using an "automatic thickness offset" feature that forces the material shutter to close a bit before the nominal thickness is measured. Unfortunately, there is no discernable trigger for this action and it is not adjustable by the user, rendering this technique unreliable. The heat

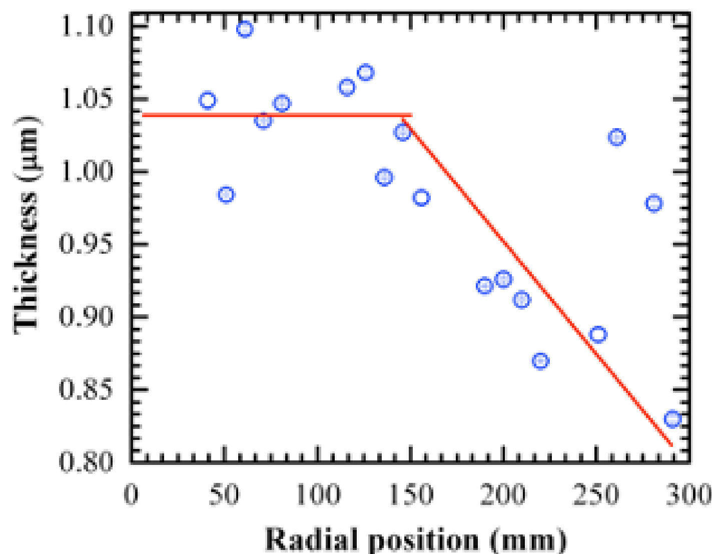

Figure 5: Measured film thickness (nominal 1 µm) as function of distance from the caousel center

deposited during evaporation is carried only in part by the deposition flux of ad-atoms which, having spent some energy in evaporation or sublimation, are relatively cold. Much of the effect is caused by the heat radiated by the material in the crucibles. Thus, the reduction of the thermal shock requires a decrease of the power density on the target material while maintaining a desired 1 Å/s deposition rate. There are two classes of materials requiring two different strategies. For materials that melt fully, like Titania and Tantala, it is useful to use a smaller crucible containing less material and requiring less heating for evaporation. These materials hardly require any sweep of the e-beam on the surface due to the good thermal conductivity of the liquid bulk. The evaporation process is almost a step function of the temperature. Once melted, a static beam spot at low power can induce the desired 1 Å/s evaporation rate even from a small surface area. On the other hand, the radiated black body power is proportional to the heated area, so a small crucible minimizes heating on the QCM and target substrates. A limited amount of e-beam power spilling at the edges of the sublimating material is of little concern because the crucible is made of Molybdenum and water cooled. The cooling keeps the Molybdenum far from its sublimation temperature. This sweep strategy mitigates fluctuations of the deposition rate, of the heating

Figure 6: Upgraded OptoTech OAC-75-RF coater with dual e-gun configuration

of substrates and QCM, and of the power of the e-gun when the feedback is active. Conversely, some materials sublimate at the target deposition rate before reaching their melting point. Sublimating materials, like fused Silica, require larger crucibles and wide beam sweeps to broaden the area of the material heated by the electron beam and ensures that no spot heats disproportionately. In the absence of a suitably large and uniform sweep, the concentrated sublimation creates a hole in the material which modifies the shape of the plume and decreases the effective sublimation rate, as well as changing the heat irradiation pattern on the QCM. If the deposition rate feedback is active, the decreased rate will cause the e-gun to increase power in response, which further deepens the hole. If the deposition rate feedback is turned off, the deposited thickness creeps lower layer after layer. Wide and uniform beam sweeps, uniformly heating the sublimating material's exposed surface, prevent hole production and mitigate the instabilities. Scaling factors to increase the power when the beam is aimed farther away from the center are needed to uniformed the effective power across the surface of the material. The improvements described above greatly stabilized the process but could not address the drifts in deposition rate occurring when the feedback must be switched off during the long times required to deposit many thin layers. For these thin layers the standard feedback must be off because the QCM thermal shock would produce and correct for false deposition rate measurements. A software strategy was devised to further improve this issue. New software introduced the ability to automatically adjust the deposition time by using the information that can be gathered monitoring the thicknesses of previously deposited layers. Though the new software still relied on QCM measurements, there is a fundamental difference; rather than making measurements during the deposition, it considers only the QCM frequency when the shutter is first opened and still unaffected by the thermal shock, or when the shutter closes and the QCM is still hot. The actual deposited thickness of each layer can be computed by comparing the corresponding frequency of the previous layer. This strategy was first implemented to increase or decrease the length of subsequent layer deposition times with the aim of obtaining the nominal thickness. This of course works only if the deposition times for each nanolayer are long compared with the rotation period. A more complicated incremental adjustment of the deposition speed (e-beam current) together with synchronization of the shutter operation with the carousel position was needed. It was at this time that the ability to synchronize the shutter to the carousel position was added to the software. There have been

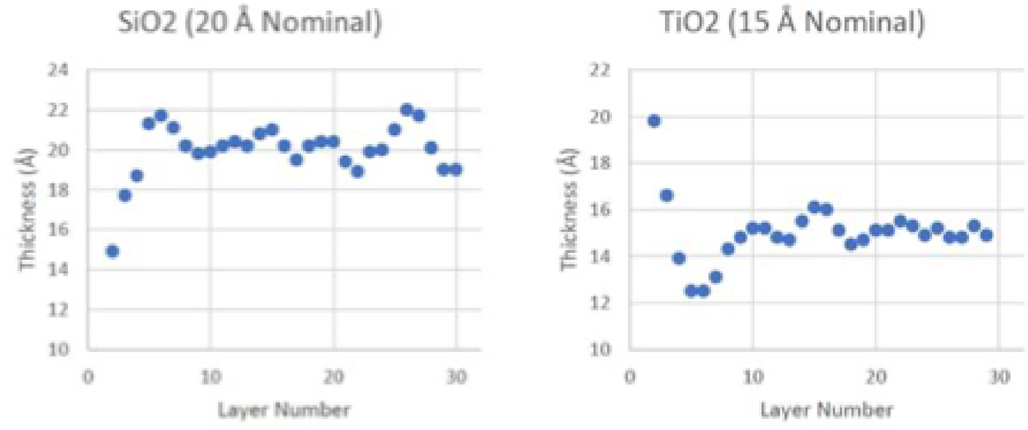

Figure 7: Measured layer thicknesses for SiO_2 and TiO_2. The layer-correcting software starts after three layers. Before that, trends are due to the coater auto-adjusting power to achieve desired deposition rates.

dramatic improvements in the quality, accuracy, and consistency of coatings with only the addition of the second e-gun, the software upgrades, and the new deposition and feedback strategies. A 59-layer TiO_2-SiO_2 test deposition was made to assess the system. Plots of the measured layer thicknesses according to the QCM show the behaviour of the thickness correcting software (Figure 7). The correcting process began after the third layer of each material and immediately started making improvements. This process is the newest version of the software which considers the nominal layer thicknesses in addition to the nominal total thickness. The measured values (taken from the crystal cold states) and nominal values are about 1 Å apart by the end of the coating, as is the total desired thickness.

Figure 8 shows three samples. The sample on the left was made prior to the installation of the second e-gun, though it used an early version of the thickness-correcting software. The middle sample was made with the same recipe but with the additions of the second e-gun and updated thickness-correcting software. The right sample was also made with the second e-gun and updated software, but it used a different recipe designed to be optically equivalent to the first. Despite being a different coating recipe, the middle and right samples are more similar in colour, indicating that the nominal thicknesses are correct. Samples made prior to the upgrades, even if nominally identical, showed very different colours.

Figure 8: Optically equivalent coatings on 2” Si substrates. The coating on the left was made before the addition of the second e-gun. The middle and right coatings are far better optical matches

The coatings described in Tables 2 are part of a set of prototypes made with the showed up-to-date software and hardware systems.

High Index	**Number of Layers**	**Nominal Thickness** (nm)	**Total Thickness** (nm)
SiO_2 TiO_2	76	1.3 2	125.4
SiO_2 TiO_2	82	1 2	123
Ta_2O_5 TiO_2	68	1.4 2	115.6
ZrO_2 TiO_2	62	1.7 2	114.7
Al_2O_3 TiO_2	78	1.1 2	120

High Index	**Number of Layers**	**Nominal Thickness** (nm)	**Total Thickness** (nm)
Al_2O_3 SiO_2	78	1.1 2	120.9

Table 2: Prototype samples derived from nanolayer optimization algorithm.

Structural, compositional and morphological characterization of the films

The work done in the frame of the EGO AdV+ fellowship has also been focused on the structural and compositional characterization of the deposited films. In particular, the atomic force microscopy (AFM), X-ray diffraction (XRD), X ray reflectivity (XRR), Raman spectroscopy (RS) and transmission electron microscopy (STEM) facilities was available to the UniSa Virgo/ET Groups, that work in close collaboration with the UniSannio Colleagues, as detailed below.

Instrumental facilities

AFM images have been acquired with a Nanowizard III, equipped with Vortex electronics from JPK (Berlin, DE), in the standard tapping mode technique, using a SCM-PIT-V2 tip from Bruker (Billerica, MA, USA). The cantilevers used were characterized by means of force curve spectroscopy and thermal methods, resulting in a resonance frequency and elastic constant of $f_0 \approx 75kHz$ and $k \approx 3N/m$, respectively. The surface morphology was analyzed by a field emission scanning electron microscope (FESEM) from ΣIGMA Zeiss, with a nominal resolution of 1.3 nm at 20 kV. The high-resolution SEM micrographs have been acquired using an InLENS detector with an acceleration voltage of 10 kV, a working distance of 5 mm and a beam current of 80 µA. The film composition X-ray microanalysis was performed by energy dispersive spectrometry (EDS) using an Oxford-Inca Energy 300 system to check chemical composition and absence of contamination in as deposited and annealed films. In order to study the structural properties, X-ray diffraction analysis was performed on as-grown and annealed nanolayers. All the samples have been analysed using a diffractometer from Bruker to check the emergence of crystallinity as a function of annealing temperature. X-ray analysis with a high-resolution Philips X-Pert MRD diffractometer was also carried out using monochromatic $Cu - K_{\alpha l}$ radiation with wavelength of 0.154056 nm. The diffractometer was equipped with a four crystal Ge220 asymmetric monochromator and a graded parabolic mirror positioned on the primary arm which reduces the incident beam divergence to 0.12 arc-sec. Post deposition analyses, based on X-ray reflectivity (XRR), were performed to confirm the effective thickness of the investigated samples, together with

profilometry, by using Alpha-Step D-600. A Raman Spectrometer, in the backscattering geometry, was used to exploit the structural and vibrational properties of the investigated samples. A near infrared laser, with a wavelength of 785 nm, was used as the excitation source.

Amorphous to crystalline transition studies

During the research activity carried out in this project, the amorphous-to-crystalline transition of thin films during post-deposition annealing was thoroughly investigated, as a function of both film thickness and of the maximum annealing temperature (between 250 and 1000°C)[21]. Crystallization upon annealing is a common feature of most candidate optical materials proposed so far (the only exceptions being likely Silica and Alumina), the only difference being the temperature at which crystallization occurs. However, it has been known for long that either doping with a stable glassy material (e.g., Silica) or reducing film thickness reduction down to a few nm, effectively increases the annealing temperature at which crystallization sets in. For brevity we shall present here only the results for Silica-Titania (high-idex) and Silica-Alumina (low-index) nanocomposites.

The annealing facility

The as deposited samples have been heat treated in air. The annealing treatments were carried out in a Carbolite muffle furnace (model RHF 15 - T_{max} 1500°C) and in a "home made" furnace where the heater is placed in a stainless-steel chamber. Both furnace are controlled by a proportional-integral-derivative (PID) system. The samples were heated with a rate of 3°C/min, up to a temperature of 250, 300, 400, 450, 500, 600, 800, 1000°C, and left at fixed T for 12 h. Finally, they were cooled down to room temperature with a rate of 1°C/min. In Figure 9 are reported the two system used for the annealing procedure.

Crystallization indicators

Both XRR and RS were used to detect the onset of crystallization. XRD measurement and Raman spectroscopy of a nanolayered TiO_2/SiO_2 composed of 76 layers as grown are reported in Figure 10. Both spectra show

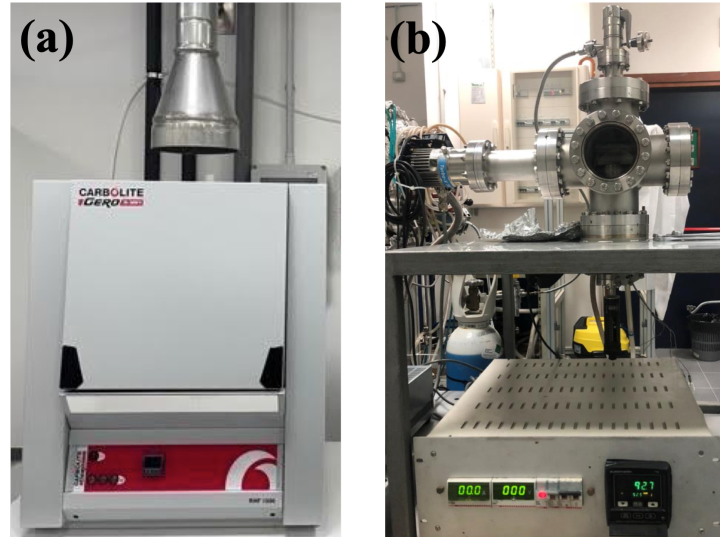

Figure 9: (a) Carbolite muffle furnace (model RHF 15) and (b) "home made" furnace.

only the peaks of the crystalline Si substrate, demonstrating that the deposited film is amorphous. In Figure 11 Raman spectroscopy of the same a nanolayered as grown and at two different annealing temperatures, 500°C and 700°C. At 700°C a peak related to the crystallization of TiO_2 appears. The same type of study was conducted on the other deposited nanolayered, with high index, and all the results obtained are summarized in Table 3. It is possible to conclude that the onset of crystallization occurs between temperatures of 500°C and 700°C.

The same type of analysis was also performed on the nanolayer with low refractive index, Al_2O_3/SiO_2, in this case the crystallization temperature is higher. Figure 12 shows the X-ray diffraction spectra at different temperatures, at 1000°C the diffraction peaks of the crystallization of Al_2O_3 are observed. The details of the structure of this nanolayer are shown in Table 4. As expected, in view of the glass-forming nature of both materials, Silica/Alumina nanocomposites remain amorphous up to extremely high annealing temperatures (> 700°C).

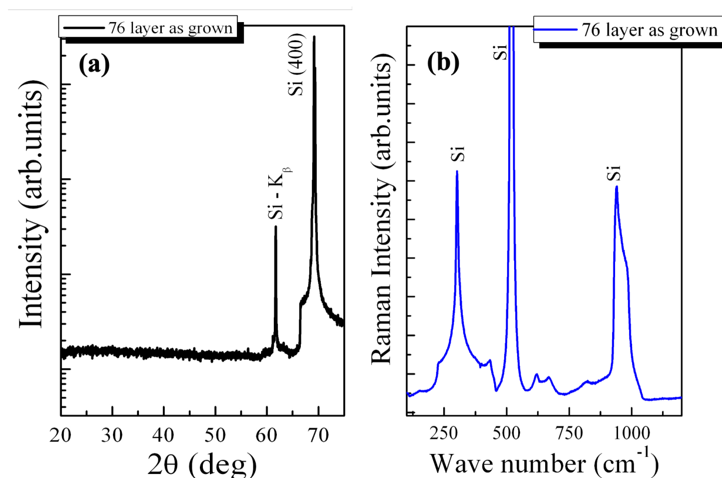

Figure 10: (a) XRD measurement and (b) Raman spectroscopy of a nanolayered TiO_2/SiO_2composed of 76 layers as grown. Both spectra show only the peaks of the crystalline Si substrate.

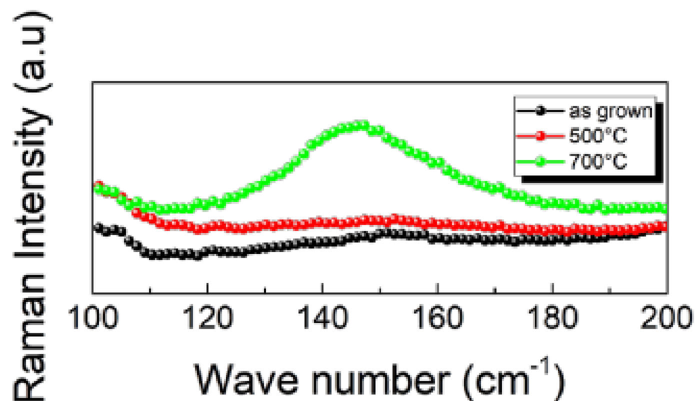

Figure 11: Raman spectroscopy of a nanolayered TiO_2/SiO_2composed of 76 layers as grown and at two different annealing temperatures, 500°C and 700°C.

High Index	Number of Layers	Layer Thickness (nm)	Cryst. T (°C)
SiO_2 TiO_2	76	1.3 2	500-700
SiO_2 TiO_2	82	1 2	500-700
Ta_2O_5 TiO_2	68	1.4 2	500-700
ZrO_2 TiO_2	62	1.7 2	500-700
Al_2O_3 TiO_2	78	1.1 2	500-700

Table 3: Crystallization onset of High index nanolayers

High Index	Number of Layers	Layer Thickness (nm)	Cryst. T (°C)
Al_2O_3 SiO_2	78	1.1 2	700-1000

Table 4: Crystallization onset of Low index nanolayer Al_2O_3/SiO_2.

Morphological/Structural Characterization

Prototypes of non-crystallized quarter-wavelength thick films where characterized in terms of their morphological, structural and optical properties using our AFM, XRR, and STEM facilities. As an illustration, here we shall focus on nanolayered Silica/Titania prototypes consisting of 38 TiO_2 and 38 SiO_2 layers (alternating), and nanolayered Silica/Alumina prototypes consisting of 39 SiO_2 layers and 39 Al_2O_3 layers. Both films where a quarter of wavelength thick at 1064 nm, in correspondence of their nominal design index. These configurations were identified as the non-crystallizing designs featuring the thinnest feasible layers of the two materials and the largest

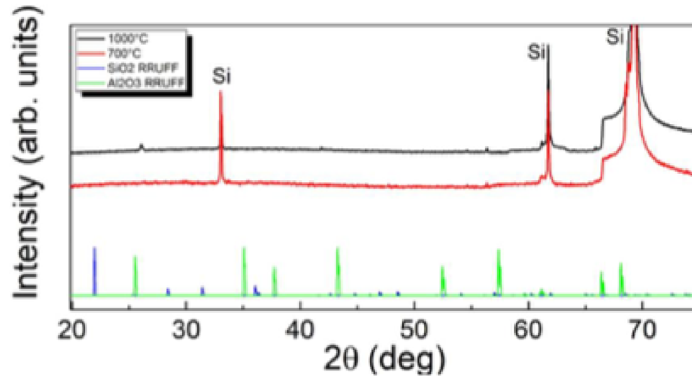

Figure 12: XRD spectra of a nanolayered Al_2O_3/SiO_2 composed of 78 layers two different annealing temperatures, 700°C and 1000°C

optical contrast.

AFM Topography

Figure 13 displays the tapping-mode AFM topography with a scan area ranging from 10 µm x 10 µm to 20 µm x 20 µm, of the Silica/Titania (76 layers) sample as function of the annealed temperature (T_a). These topographies indicate a surface roughness that changes as the annealing temperature increases. By increasing T_a up to 700°C the surface preserves its flatness (with an RMS lower than 1 nm), whereas it becomes corrugated, as formed by small faceted grains, upon annealing at 1000°C. Thus, the RMS roughness jumps from 1 nm to 4 nm. AFM measurements were also carried out for the sample of 78 layers of Al_2O_3/SiO_2.

Figure 14 display the temperature evolution of the topography showing a surface that stays unchanged up to 700°C, while is profoundly modified by the annealing at 1000°C. This result is further confirmed by the RMS roughness which stays lower than 2 nm up to 700°C, and then increases above 10 nm at 1000°C.

X-RAY Reflectivity

Using XRR it was possible to estimate the thickness of the individual layers, and the roughness of the interfaces between adjacent layers. Figure 15 shows the measurements and pertinent fit, and Table 5 resumes the results. The

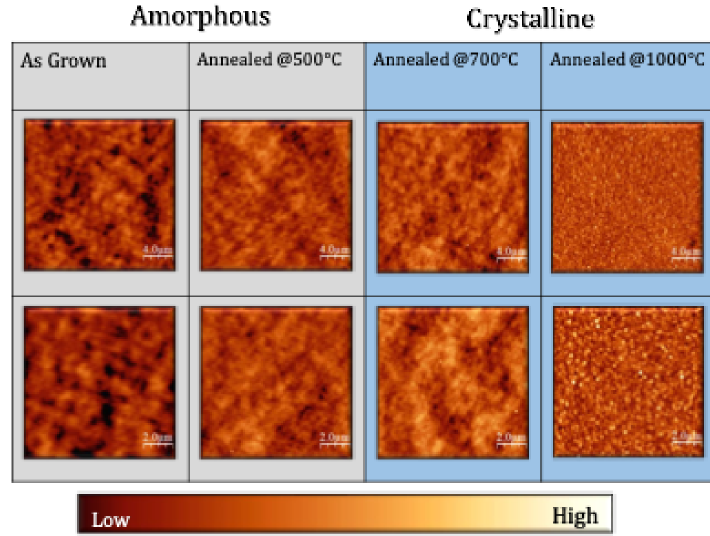

Figure 13: Tapping mode AFM topography of as-deposited nanolayered TiO_2/SiO_2 film at different annealing temperatures. The color scale ranges from 0 to 10 nm.

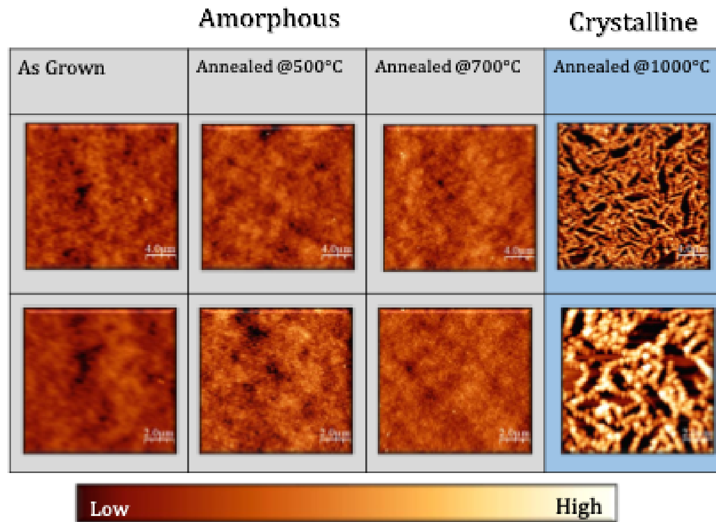

Figure 14: Tapping mode AFM topography of as-deposited nanolayered Al_2O_3/SiO_2 film at different annealing temperatures.

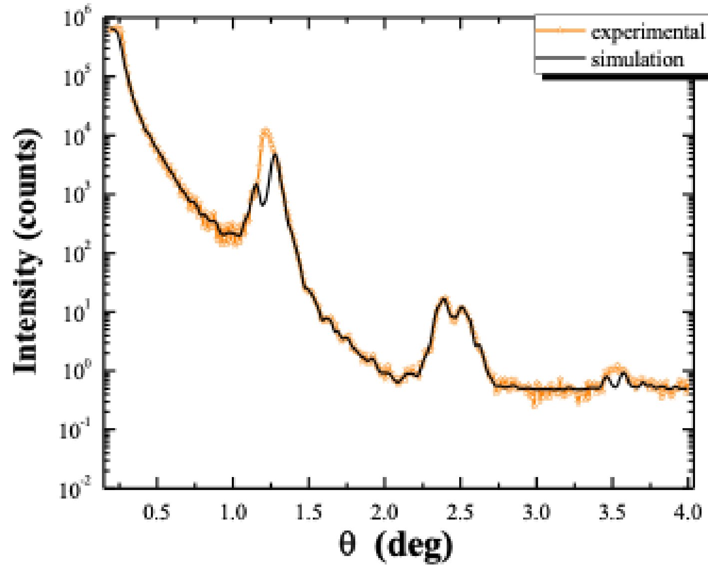

Figure 15: XRR measurement of a TiO_2/SiO_2 film composed of 76 layer and relative fit.

latter are in agreement, within the experimental errors, with the thicknesses measured by the OAC-75RF QCMs during deposition; and the estimated interface roughness is nicely low.

	Thickness d(nm)	**Roughness** σ(nm)
Si substrate		0.6 ± 0.3
TiO_2	2.10 ± 0.09	0.4 ± 0.1
SiO_2	1.4 ± 0.1	0.4 ± 0.1

Table 5: Estimated thicknesses and roughness of the nanolayered film consisting of 76 layers of TiO_2 and SiO_2 obtained by XRR measurements

The same type of measurement was also carried out on the other nanolayers, both those with High Index and Low Index ones, but their analysis is in progress.

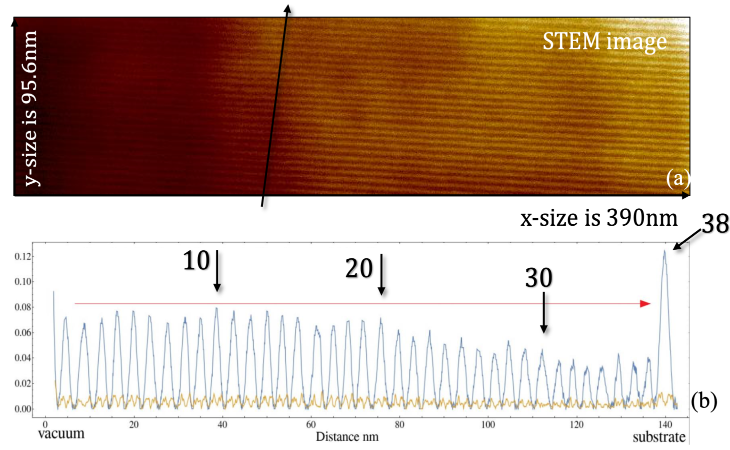

Figure 16: (a) STEM image of 76-layer TiO_2/SiO_2 sample showing well-defined nanolayers with low interdiffusion. (b) Line profile from the STEM. Blue peaks represent intensity with background removed. The yellow line corresponds to the roughness.

STEM Analysis

To complete the investigation on both samples periodicity and thicknesses, cross sectional analyses have been performed by means of a scanning transmission electron microscope (STEM). The STEM image acquired on the 76 layers, along a scan area of 390 nm x 95.6 nm, is showed in Figure 18 (a). Clearly, all the 76 layers are correctly formed, as they can be counted and numbered. Moreover, the analysis of the STEM image can be used to evaluate the periodicity, the thicknesses of each single layer, as well as the total one, to be compared with the one measured by XRR. Figure 18 (b) shows the depth profile measured along the dashed line traced in panel (a). After the first region corresponding to the air the fabricated nanostructures become visible counting a number of 38 TiO_2/SiO_2 doublets with a total thickness of 143.16 nm. Currently the STEM analysis has been carried out only on this nanolayer, but analyses have also been scheduled on the other samples at the University of Salerno.

Optical Properties

Optical Ellipsometry characterization of the above-mentioned prototypes was performed, in the frame of the VCRD by the ET/Virgo group of INFN-

Genova by Michele Magnozzi. The measurements are reported in Figure 19. Blind retrieval of the individual layers thicknesses and indexes is blurred by a very large reconstruction error. On the other hand, using the layer thicknesses estimated from XRR and STEM measurements, the layer index spectra fit well the nominal values obtained from mixture theory. In Salerno we built an optical characterization setup wich follows a different scheme, and it is illustrated in details in following section.

Optical Characterization

Generally, in composite structures, for the calculation of the equivalent refractive index, the Drude formula or mixture formula is used, which however cannot be used for a nanostratified structure. In fact, it can be demonstrated that a multilayer medium composed of isotropic layers with a much smaller period than the wavelength is equivalent to a uniaxial homogeneous anisotropic medium with optical axis normal to the surfaces [22]. Then the multilayer can be modeled as a single uniaxial anisotropic medium with ordinary and extraordinary refractive indexes that can be calculated analytically with a certain degree of approximation in the limit where the layers are thin enough. The calculation of the ordinary and extraordinary refractive indices, however, requires knowledge of the refractive indices thicknesses of the constituent materials.

The technique proposed albeit presents some theoretical glitches has been verified that works well under certain assumptions. In addition, this technique has the advantage of being easy to implement in a laboratory, with the drawback of being able to apply it to a single wavelength.

It was developed by Abelès [23] in 1949, and since then, research on it has been ongoing [24] [25]. As a result, its key characteristics are well understood. The technique is based on the principle for that p-polarized incident light, when it is incident at the Brewster angle of the film, entirely transmits through the surface of the film, as if the film is not being "seen".

As a result, the Brewster angle is the angle for which the transmittance spectrums for p-polarized incidence of the film and of the substrate alone cross.

The ray, in fact, undergoes the effects of the film medium, namely, it is bent by refraction, but it does not experience energy loss and does not bounce back and forth in the film as is typical.

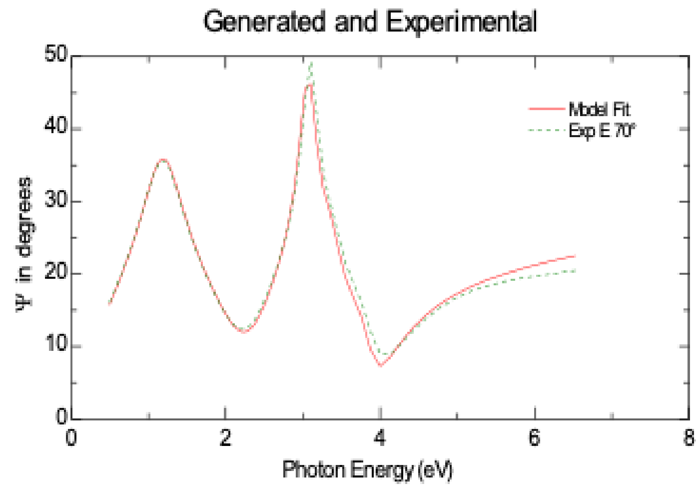

(a)

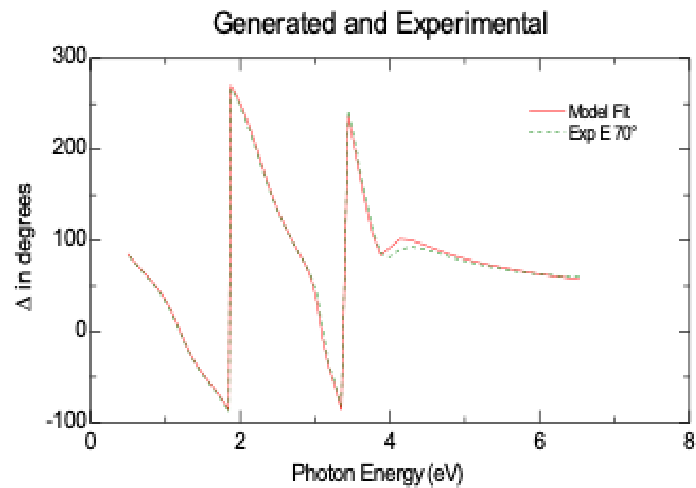

(b)

Figure 17: Ellipsometry spectra (markers, green) and best-fit simulations (lines, red) of TiO_2/SiO_2nanolayered coating.

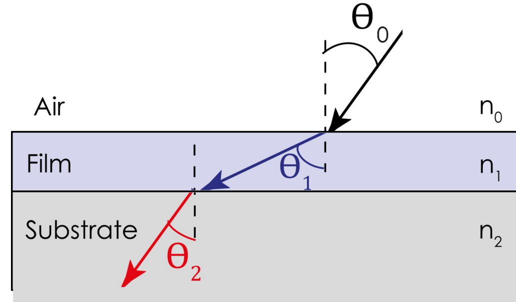

Figure 18: Model of Multilayers structure under test

Let us consider a structure consisting of two homogeneous dielectric half-spaces with refractive indices of n_0 and n_2, respectively, and a thin layer with refractive index n_1 sandwiched between them (see Figure 18). The substrate is the half-space to the bottom (with refractive index n_2), while the vacuum is the half-space to the top.

Let a monochromatic plane wave impinge with an incidence angle θ_0 on the coating from the vacuum, part of this wave will be transmitted inside the film and will be incident on the interface with the substrate with an angle of incidence θ_1.

Assuming that the substrate is much thicker than the penetration depth it can be assumed to be semi-infinite, so that in the substrate there will be only the transmitted wave that propagates endlessly with the angle θ_2.

The field reflection coefficient for this structure can be found in many textbooks (e.g., refs. [26]), and is sometimes referred to as the Fresnel-Airy formula:

$$\Gamma = \frac{\Gamma_{01} + \Gamma_{12} e^{-2i\delta_1}}{1 - \Gamma_{01}\Gamma_{12} e^{-2i\delta_1}} \tag{2}$$

where

$$\Gamma_{ij}(\theta_i) = \frac{\tan(\theta_j - \theta_i)}{\tan(\theta_j + \theta_i)}$$

is the polarization-dependent Fresnel coefficient and

$$\delta_1 = \frac{2\pi}{\lambda} n_1 d_1 \cos\theta_1$$

The fraction of light that is reflected is described by the Fresnel equations and depends on the incoming light's polarization and angle of incidence. The

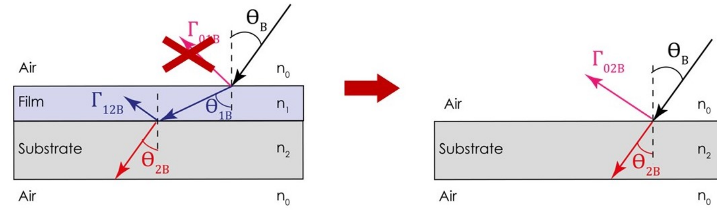

Figure 19: Schematic of the reflection at Brewster's angle incidence

Fresnel equations predict that light with the p-polarization (electric field vector lying in the same plane defined by the incident ray and the vector normal to the surface) will not be reflected if the angle of incidence is the *Brewster's angle*

$$\theta_B = \theta_0 = \tan^{-1}\left(\frac{n_1}{n_0}\right) \tag{3}$$

It can be shown that, at the Brewster's angle, the Fresnel reflection coefficient for the interface between the film under test and the substrate is equal to the Fresnel reflection coefficient at the Air-Substrate interface. In terms of reflectance, it can be said that, at the Brewster angle, the reflectance of the entire system under test (Air-Film-Substrate) is equal to the reflectance of the structure composed of Air-Substrate:

$$|\Gamma_B|^2 = |\Gamma_{02B}|^2 \tag{4}$$

Experimental Validation

In order to experimentally validate the Experimental Method an optical setup to measure angular reflectance spectra of deposited samples has been built and it is shown in Figure 20.

A laser source, at a wavelength of $632.8nm$, passes through a polarizer (which only transmits the p-polarized waves to identify the Brewster angle) and a $100\mu m$ pin-hole with the purpose of conveying the incident wave and having a collimated ray. The emerging wave is incident on the sample placed on a rotator with a graduated ring that allows you to measure the reflected power transmitted through a photometer as the angle varies.

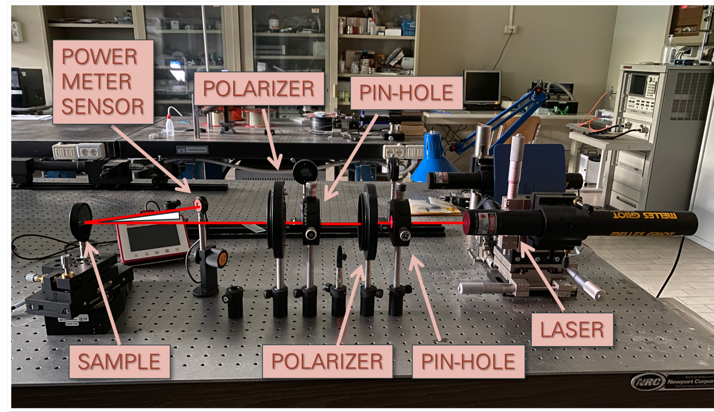

Figure 20: Measurement setup for angular characterization

Therefore, it was possible to obtain the refractive index of the film under consideration by measuring the reflectance of the substrate (Air-Substrate interface alone) first, and measuring the reflectance of the system composed of Air-Film-Substrate afterwards. Then, with a Matlab routine, the two curves of the reflectance were reconstructed as the angle of incidence changed; they were superimposed and the intersection between the two curves was found, which occurs precisely in correspondence of the Brewster angle.

Finally, by exploiting the inverse equation of the definition of the Brewster angle, it was possible to know the refractive index of the film under test provided that the substrate refractive index is known with a certain accuracy.

Calibration of the measurement setup

In order to calibrate the measurement setup described in the previous section, it has been tested the efficiency of the setup by measuring the angular reflectance spectrum on a known film made of a layer of TiO_2 200 nm thick deposited on a silicon substrate 2 mm thick, as illustrated in Figure 21. After retrieving the refractive index of the TiO_2 layer by means of the Abelès Method it has been compared against a reference value [27].

Characterization of TiO_2 layer

The angular reflectance of the silicon substrate alone were measured along with the reflectance of TiO_2 layer deposited on the same silicon substrate

Figure 21: Schematic of TiO_2 layer on Si substrate.

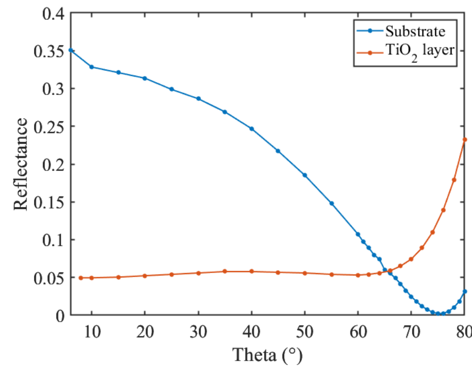

Figure 22: Measured reflectance of: TiO_2 layer on Si substrate (red curve) and substrate alone (blue curve).

(see Figure 22). Following the Abelès Method it has been found an intersection of the two curves at angle $\theta = 65.66°$, making an interpolation of the measurement data. Using the equation (3) the refractive index of the thin film titania layer has been found to be $n_{film} = 2.21 \pm 0.07$, which is consistent with the reference value [27]. The uncertainty in the value of n_{film} is due to the accuracy of the measurement setup which is $\pm 1°$.

The angular reflectance calculated with the n_{film} value has been superimposed to the measured one finding an excellent agreement, as depicted in Figure 23. The reflectance of the structure is calculated using the Transmission Matrix Method [28].

Characterization of TiO_2/SiO_2 Nanolayers

TiO_2/SiO_2 NLs deposited on Si substrate by using IAD have been optically characterized by means of Abelés Method. The number of layers, the nominal thickness, d_{nom}, (i.e thickness set during the deposition phase) of the single

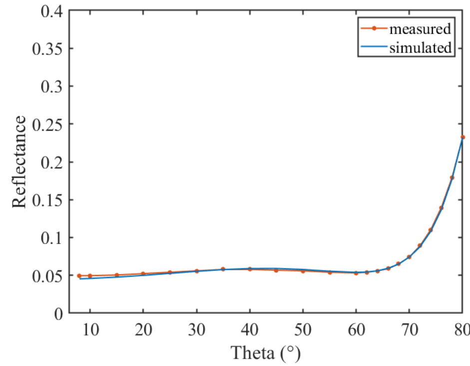

Figure 23: Comparison between the measured reflectance of TiO_2 layer on Si substrate (red curve) and the reflectance of the equivalent layer (blue curve).

layer and the total nominal thickness of the coating are shown in Table 6. The results of these characterizations are summarized in the following Table 7

N* Layer	**Thickness**		
	SiO_2	TiO_2	Coating
76-layers	13 $\AA$	20 $\AA$	125.4 nm
82-layers	10 $\AA$	20 $\AA$	123 nm

Table 6: Parameters of TiO_2/SiO_2 nanolayers: number of layers, nominal thickness, d_{nom}, (i.e thickness set during the deposition phase) of the single layer and total nominal thickness

where θ_B is the Brewster's angle, n_{eq} the equivalent refractive index, d_{fit} is the thickness of the equivalent layer falling under the range of uncertainty which best reproduce the measured reflectivity, $MSE\%$ is the Percentage Mean Square Error between the measured reflectivity and the simulated one with equivalent layer parameters.

Figure 24 shows the schematic of the structure under test, Figure 25a and Figure 25b the Angular reflectance spectrum and the application of Abelès Method of the 76-nanolayers and 82-nanolayers, respectively. Figure 26a and Figure 26b show the measured spectrum reflectivity and the one simulated by a Matlab routine of the nanolayer structure made of equivalent layer with

Layer	θ_B	n_{eq}	d_{fit}	MSE%
76-layers	64.7	2.1155	116.15 nm	4.20×10^{-3}
82-layers	64.8	2.1251	112.60 nm	1.49×10^{-3}

Table 7: Parameters of equivalent layer of TiO_2/SiO_2 nanolayers: Brewster's angle θ_B, equivalent refractive index, n_{eq}, depth of the Abelés equivalent layer d_{fit} and Percentage Mean Square Error, $MSE\%$, between the measured reflectivity and the simulated one with equivalent layer parameters.

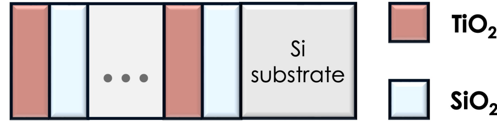

Figure 24: Schematic of TiO_2/SiO_2 nanolayer structure.

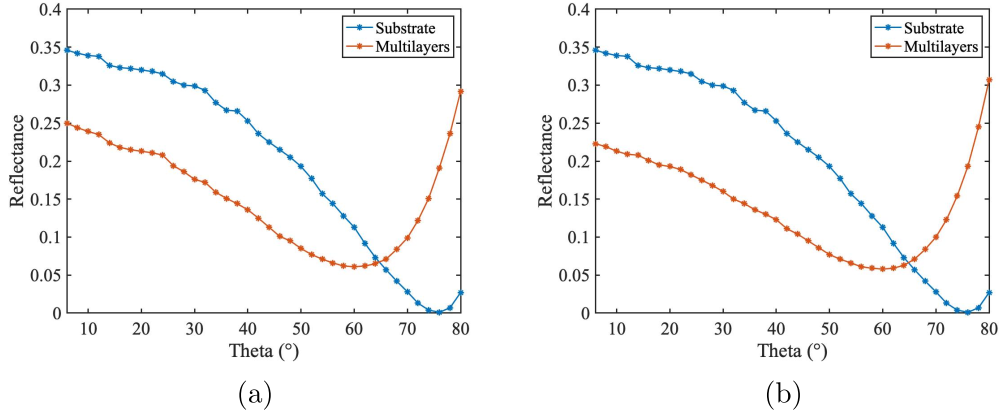

Figure 25: Measured reflectance of: TiO_2/SiO_2 nanolayers (red curve) and substrate alone (blue curve). (a) 76 layers; (b) 82 layers.

n_{eq} and d_{fit} reported in Table 7. The d_{fit} value of the 76-nanolayers and 82-nanolayers is consistent with the x-ray measurements of the nanolayers made by the collaboration, $d_{XRD} = 110 \pm 2nm$ and $d_{XRD} = 118 \pm 6nm$, rispectively. It is important to point out that the control of thickness is crucial to reach the desired optical properties of the prototype. In fact, it is possible to see that small variations of thickness may cause remarkable differences in the

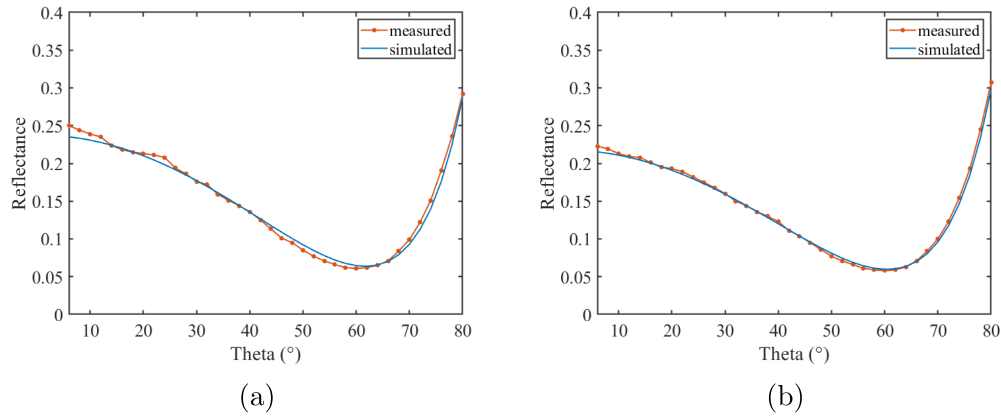

Figure 26: Comparison between the measured reflectance of TiO_2/SiO_2 nanolayers (red curve) and the reflectance of the equivalent layer (blue curve). (a) 76 layers; (b) 82 layers.

refractive index of the nanolayer.

Characterization of TiO_2-based Nanolayers

NLs formed by alternating TiO_2 with Ta_2O_5, Al_2O_3, and ZrO_2 are analyzed by adopting the same strategy as illustrated in the previous section. The oxides are characterized by a higher refractive index compared to SiO_2 at wavelength of $1064nm$, wich is the operation wavelength of the laser actually used in GWs interferometer. Indeed, the refractive index are:

- $n_{TiO_2} = 2.3894$
- $n_{Ta_2O_5} = 2.1200$
- $n_{Al_2O_3} = 1.6773$
- $n_{ZrO_2} = 2.1517$
- $n_{SiO_2} = 1.4636$

The nominal thickness of low- and high-index material layers constituting the analyzed NLs are reported in the Table 8 along with the total thickness of the NL coating.

No. Layer	Thickness		
	L-index	H-index	Coating
62-layers	ZrO_2	TiO_2	
	17 $\AA$	20 $\AA$	114.7 nm
68-layers	Ta_2O_5	TiO_2	
	14 $\AA$	20 $\AA$	115.6 nm
78-layers	Al_2O_3	TiO_2	
	11 $\AA$	20 $\AA$	120.9 nm

Table 8: Parameters of TiO_2-based nanolayers: number of layers, nominal thickness, d_{nom}, (i.e thickness set during the deposition phase) of the single layer and total nominal thickness

Measurements of the reflectance spectrum have been conducted on such NLs finding, for each of them, the value at which the reflectivity spectrum matches the one of the substrate alone, see Figures 28.

The values of the angles at which it occurs are reported in the third column of the Table 9. The calculated equivalent refractive index is reported therein.

L-index	H-index	θ_B	n_{eq}	d_{fit}	MSE%
ZrO_2	TiO_2	66.3	2.2781	102.15 nm	1.13×10^{-2}
Ta_2O_5	TiO_2	66.6	2.3109	105.40 nm	2.52×10^{-2}
Al_2O_3	TiO_2	64.3	2.0778	115.55 nm	6.40×10^{-2}

Table 9: Parameters of equivalent layer of TiO_2-based nanolayers: Brewster's angle θ_B, equivalent refractive index, n_{eq}, depth of the Abelés equivalent layer d_{fit} and Percentage Mean Square Error, $MSE\%$, between the measured reflectivity and the simulated one with equivalent layer parameters.

Once the refractive index of the equivalent layer has been calculated the reflectance spectrum is then compared with the measured one using a thickness d_{fit} which provides the curve the minimum MSE%. The value of d_{fit}

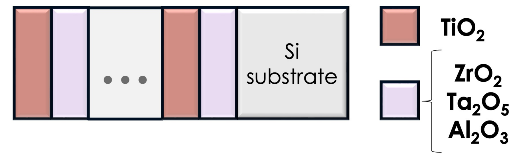

Figure 27: Schematic of TiO_2-based nanolayers.

– which always falls into the uncertainty range of the thickness of the NLs deposited – and the MSE% are reported in the Table 9.

As it can be seen from Figures 29 there is an excellent agreement between the simulated curves using the parameters obtained by the Abelès Method and the measured ones.

Mechanical Losses and Thermal Noise

Parallel to the activity of deposition and morphological and structural characterization, a thermal noise measurement system, QDPI, Quadrature Differential Phase Interferometric, is being developed at the University of Salerno 30.

Conclusion

Ultrathin (nm-scale) layered coatings can be produced with e-beam deposition with angstrom-level precision. Our results, based on AFM, XRD, XRR, RS, STEM and optical characterization encouraged further investigation into the properties of nanolayered optical films for gravitational wave detectors and other extreme metrology applications.

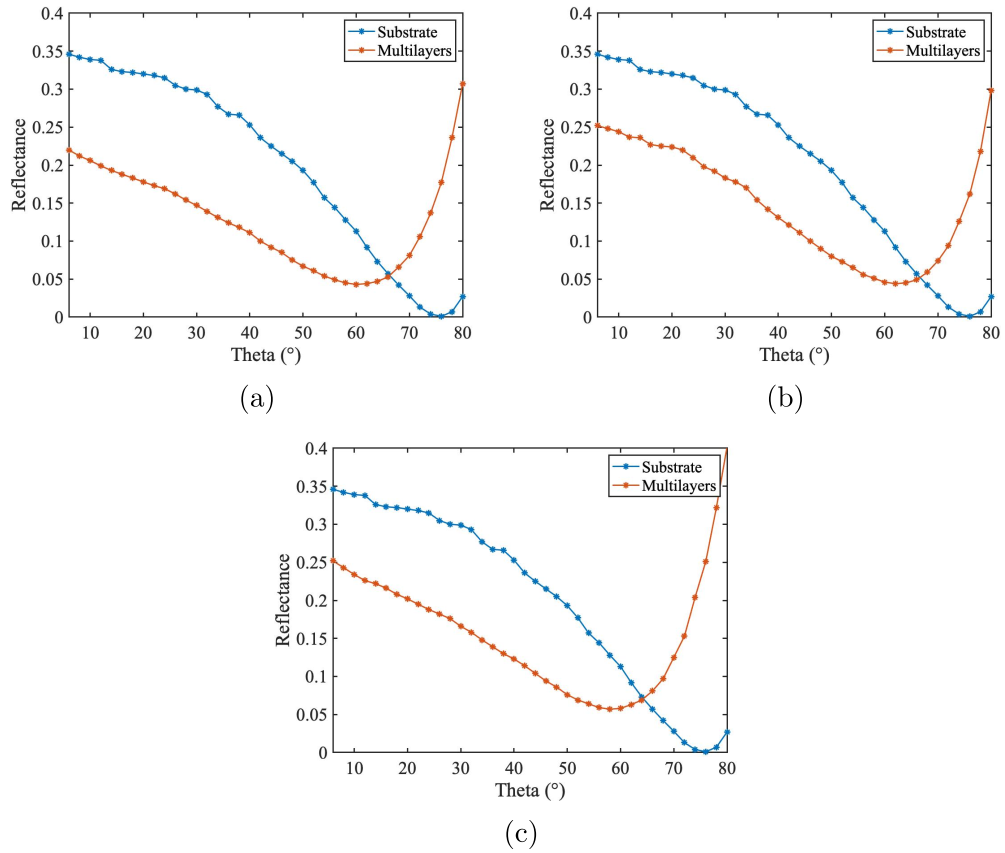

Figure 28: Measured reflectance of the nanolayers (red curve) and substrate alone (blue curve). (a) TiO_2/ZrO_2 NLs; (b) TiO_2/Ta_2O_5 NLs and (c) TiO_2/Al_2O_3 NLs.

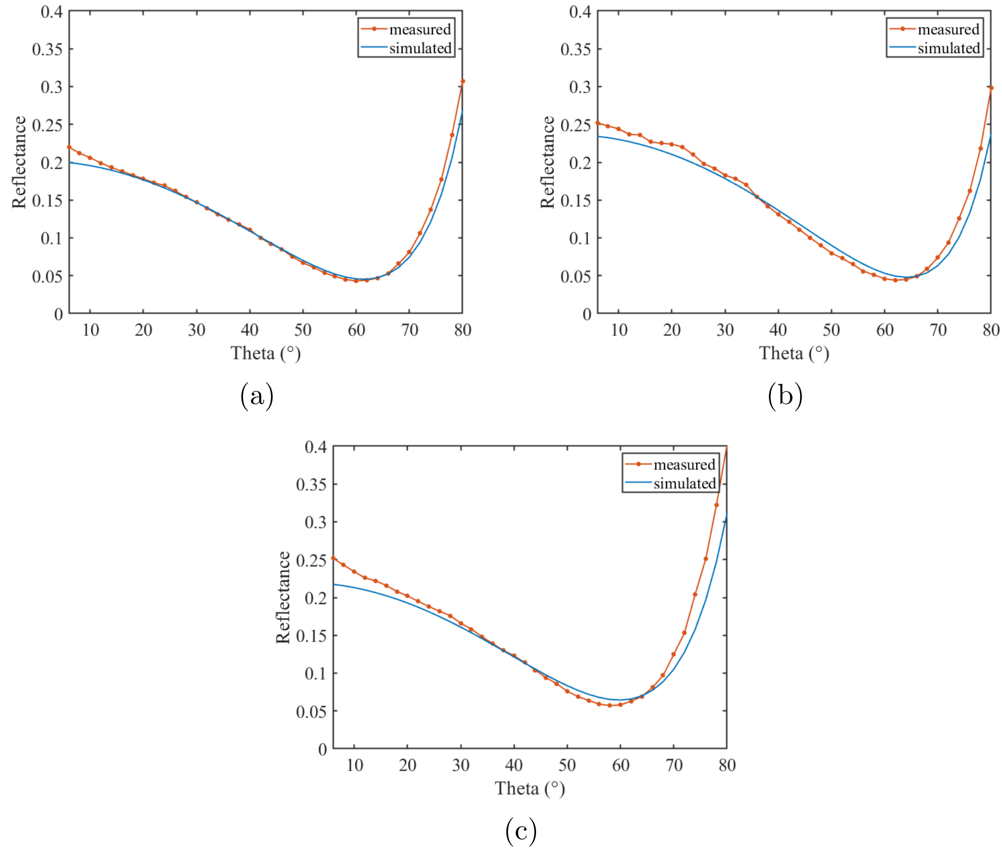

Figure 29: Comparison between the measured reflectance of the nanolayers (red curve) and the reflectance of the equivalent layer (blue curve). (a) TiO_2/ZrO_2 NLs; (a) TiO_2/ZrO_2 NLs; (b) TiO_2/Ta_2O_5NLs and (c) TiO_2/Al_2O_3 NLs.

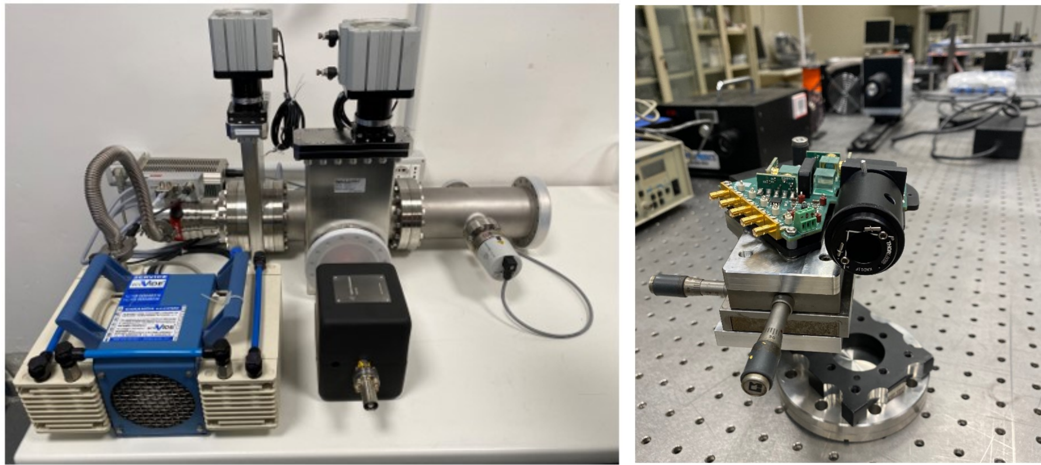

Figure 30: QDPI, Quadrature Differential Phase Interferometric, at the University of Salerno.

Bibliography

[1] Aasi, J. *et al.* (LIGO Scientific Collaboration), "Advanced LIGO," *Classical and Quantum Gravity*, vol. 32, no. 7, p. 074001, Apr. 2015.

[2] Acernese, F. *et al.*, "Advanced Virgo: A second-generation interferometric gravitational wave detector," *Classical and Quantum Gravity*, vol. 32, no. 2, Jan. 2015.

[3] Abbott, R. *et al.* (LVK Collaboration), "Observation of Gravitational Waves from a Binary Black Hole Merger," *Phys. Rev. Lett.*, vol. 116, p. 061102, Feb 2016.

[4] Abbott, R., ... and De Simone, R., *et al.* (LVK Collaboration), "All-sky search in early O3 LIGO data for continuous gravitational-wave signals from unknown neutron stars in binary systems," *Physical Review D*, vol. 103, no. 6, p. 064017, 2021.

[5] W. Hartley, "Multi-messenger Observations of a Binary Neutron Star Merger," *The Astrophysical Journal Letters*, vol. 848, no. 2, p. L12, 2017.

[6] Abbott, R. *et al.* (LVK Collaboration), "GWTC-1: A Gravitational-Wave Transient Catalog of Compact Binary Mergers Observed by LIGO and Virgo during the First and Second Observing Runs," *Phys. Rev. X*, vol. 9, p. 031040, Sep 2019.

[7] Abbott, R., ... and De Simone, R., *et al.* (LVK Collaboration), "GWTC-3: compact binary coalescences observed by LIGO and Virgo during the second part of the third observing run," *arXiv preprint arXiv:2111.03606*, 2021.

[8] Abbott, R. *et al.* (LVK Collaboration), "Population properties of compact objects from the second LIGO–Virgo Gravitational-Wave Transient Catalog," *The Astrophysical journal letters*, vol. 913, no. 1, p. L7, 2021.

[9] ——, "Tests of general relativity with binary black holes from the second LIGO-Virgo gravitational-wave transient catalog," *Physical review D*, vol. 103, no. 12, p. 122002, 2021.

[10] B. Canuel, E. Genin, G. Vajente, and J. Marque, "Displacement noise from back scattering and specular reflection of input optics in advanced gravitational wave detectors," *Optics Express*, vol. 21, no. 9, pp. 10 546–10 562, 2013.

[11] Harry, G. *et al.*, "Titania-doped tantala/silica coatings for gravitational-wave detection," *Classical and Quantum Gravity*, vol. 24, no. 2, p. 405, 2006.

[12] Pinard, L. *et al.*, "Toward a new generation of low-loss mirrors for the advanced gravitational waves interferometers," *Optics letters*, vol. 36, no. 8, pp. 1407–1409, 2011.

[13] Pierro, V. *et al.* , "On the Performance Limits of Coatings for Gravitational Wave Detectors Made of Alternating Layers of Two Materials," *Optical Materials*, vol. 96, p. 109269, 2019.

[14] Agresti, J. *et al.*, "Optimized Multilayer Dielectric Mirror Coatings for Gravitational Wave Interferometers," in *SPIE Optics + Photonics*, 2006.

[15] Kondratiev, NM. *et al.*, "Thermal noise and coating optimization in multilayer dielectric mirrors," *Physical Review D*, vol. 84, no. 2, p. 022001, 2011.

[16] Pan, H. *et al.*, "Thickness-Dependent Crystallization on Thermal Anneal for Titania/Silica nm-Layer Composites Deposited by Ion Beam Sputter Method," *Optics Express*, vol. 22, no. 24, pp. 29 847–29 854, 2014.

[17] Li, L. *et al.*, "Extreme ultraviolet resist materials for sub-7 nm patterning," *Chemical Society Reviews*, vol. 46, no. 16, pp. 4855–4866, 2017.

[18] N. Chkhalo, E. Kruglyakovand, and E. Semenov, "Optimization of optical components of spectrometers based on multilayer mirrors for soft

x-ray radiation," *Plasma Devices and Operations*, vol. 7, no. 2, pp. 123–132, 1999.

[19] I. Pinto and UniSannio/UniSA, "Nanolayered Silica/Alumina Composites," *Report Number TDS: VIR-0040A-22, DCC: LIGO-G2001499 14/09/2020*.

[20] ——, "Nanolayers Re-Thought," *Report Number TDS: VIR-0727A-21, DCC: LIGO-G1902307 09/12/19*.

[21] Durante, O. *et al.*, "Emergence and evolution of crystallization in TiO_2 thin films: A structural and morphological study," *Nanomaterials*, vol. 11, no. 6, p. 1409, 2021.

[22] C. Gu and P. Yeh, "Form birefringence of layered media and volume gratings," *JOSA B*, vol. 12, no. 6, pp. 1094–1099, 1995.

[23] Abelès, "VI Methods for Determining Optical Parameters of Thin Films," ser. Progress in Optics, W. E., Ed. Elsevier, 1963, vol. 2, pp. 249–288.

[24] J. Goell and R. Standley, "Effect of Refractive Index Gradients on Index Measurement by the Abelès Method," *Applied Optics*, vol. 11, no. 11, pp. 2502–2505, 1972.

[25] I. Awai and J. Ikenoue, "Effect of Film Transition Layers on the Abelès Method," *Applied optics*, vol. 23, no. 11, pp. 1890–1896, 1984.

[26] M. Born and E. Wolf, *Principles of optics: electromagnetic theory of propagation, interference and diffraction of light.* Elsevier, 2013.

[27] "Refractiveindex.info website," https://refractiveindex.info, refractive index datbase.

[28] H. A. Macleod, *Thin-film optical filters.* CRC press, 2010.

List of Publications

Abbott, R ., *et al.* (LVK Collaboration) (2021), 'GWTC-2: compact binary coalescences observed by LIGO and Virgo during the first half of the third observing run', *Physical Review X* **11**(2), 021053.

Abbott, R., *et al.* (LVK Collaboration) (2020), 'Gravitational-wave constraints on the equatorial ellipticity of millisecond pulsars', *The Astrophysical journal letters* **902**(1), L21.

Abbott, R., *et al.* (LVK Collaboration) (2021*a*), 'All-sky search for continuous gravitational waves from isolated neutron stars in the early O3 LIGO data', *Physical Review D* **104**(8).

Abbott, R., *et al.* (LVK Collaboration) (2021*b*), 'All-sky search for long-duration gravitational-wave bursts in the third Advanced LIGO and Advanced Virgo run', *Physical Review D* **104**(10).

Abbott, R., *et al.* (LVK Collaboration) (2021*c*), 'All-sky search for short gravitational-wave bursts in the third Advanced LIGO and Advanced Virgo run', *Physical Review D* **104**(12).

Abbott, R., *et al.* (LVK Collaboration) (2021*d*), 'All-sky search in early O3 LIGO data for continuous gravitational-wave signals from unknown neutron stars in binary systems', *Physical Review D* **103**(6).

Abbott, R., *et al.* (LVK Collaboration) (2021*e*), 'Constraints from LIGO O3 Data on Gravitational-wave Emission Due to R-modes in the Glitching Pulsar PSR J0537-6910', *Astrophysical Journal* **922**(1).

Abbott, R., *et al.* (LVK Collaboration) (2021*f*), 'Constraints on Cosmic Strings Using Data from the Third Advanced LIGO-Virgo Observing Run', *Physical Review Letters* **126**(24).

Abbott, R., *et al.* (LVK Collaboration) (2021*g*), 'Diving below the Spin-down Limit: Constraints on Gravitational Waves from the Energetic Young Pulsar PSR J0537-6910', *Astrophysical Journal Letters* **913**(2).

Abbott, R., *et al.* (LVK Collaboration) (2021*h*), 'Observation of Gravitational Waves from Two Neutron Star-Black Hole Coalescences', *Astrophysical Journal Letters* **915**(1).

Abbott, R., *et al.* (LVK Collaboration) (2021*i*), 'Population properties of compact objects from the second ligo–virgo gravitational-wave transient catalog', *The Astrophysical journal letters* **913**(1), L7.

Abbott, R., *et al.* (LVK Collaboration) (2021*j*), 'Search for anisotropic gravitational-wave backgrounds using data from Advanced LIGO and Advanced Virgo's first three observing runs', *Physical Review D* **104**(2).

Abbott, R., *et al.* (LVK Collaboration) (2021*k*), 'Searches for continuous gravitational waves from young supernova remnants in the early third observing run of advanced LIGO and Virgo', *Astrophysical Journal* **921**(1).

Abbott, R., *et al.* (LVK Collaboration) (2021*l*), 'Tests of general relativity with binary black holes from the second ligo-virgo gravitational-wave transient catalog', *Physical review D* **103**(12), 122002.

Abbott, R., *et al.* (LVK Collaboration) (2021*m*), 'Upper limits on the isotropic gravitational-wave background from Advanced LIGO and Advanced Virgo's third observing run', *Physical Review D* **104**(2).

Abbott, R., *et al.* (LVK Collaboration) (2022*a*), 'All-sky, all-frequency directional search for persistent gravitational waves from Advanced LIGO's and Advanced Virgo's first three observing runs', *Physical Review D* **105**(12).

Abbott, R., *et al.* (LVK Collaboration) (2022*b*), 'All-sky search for continuous gravitational waves from isolated neutron stars using Advanced LIGO and Advanced Virgo O3 data', *Physical Review D* **106**(10).

Abbott, R., *et al.* (LVK Collaboration) (2022*c*), 'All-sky search for gravitational wave emission from scalar boson clouds around spinning black holes in LIGO O3 data', *Physical Review D* **105**(10).

Abbott, R., *et al.* (LVK Collaboration) (2022*d*), 'Constraints on dark photon dark matter using data from LIGO's and Virgo's third observing run', *Physical Review D* **105**(6).

Abbott, R., *et al.* (LVK Collaboration) (2022*e*), 'First joint observation by the underground gravitational-wave detector KAGRA with GEO 600', *Progress of Theoretical and Experimental Physics* **2022**(6).

Abbott, R., *et al.* (LVK Collaboration) (2022*f*), 'Model-based Cross-correlation Search for Gravitational Waves from the Low-mass X-Ray Binary Scorpius X-1 in LIGO O3 Data', *Astrophysical Journal Letters* **941**(2).

Abbott, R., *et al.* (LVK Collaboration) (2022*g*), 'Narrowband Searches for Continuous and Long-duration Transient Gravitational Waves from Known Pulsars in the LIGO-Virgo Third Observing Run', *Astrophysical Journal* **932**(2).

Abbott, R., *et al.* (LVK Collaboration) (2022*h*), 'Search for continuous gravitational wave emission from the Milky Way center in O3 LIGO-Virgo data', *Physical Review D* **106**(4).

Abbott, R., *et al.* (LVK Collaboration) (2022*i*), 'Search for continuous gravitational waves from 20 accreting millisecond x-ray pulsars in O3 LIGO data', *Physical Review D* **105**(2).

Abbott, R., *et al.* (LVK Collaboration) (2022*j*), 'Search for gravitational waves from Scorpius X-1 with a hidden Markov model in O3 LIGO data', *Physical Review D* **106**(6).

Abbott, R., *et al.* (LVK Collaboration) (2022*k*), 'Search for intermediate-mass black hole binaries in the third observing run of Advanced LIGO and Advanced Virgo', *Astronomy and Astrophysics* **659**.

Abbott, R., *et al.* (LVK Collaboration) (2022*l*), 'Search for Subsolar-Mass Binaries in the First Half of Advanced LIGO's and Advanced Virgo's Third Observing Run', *Physical Review Letters* **129**(6).

Abbott, R., *et al.* (LVK Collaboration) (2022*m*), 'Search of the early O3 LIGO data for continuous gravitational waves from the Cassiopeia A and Vela Jr. supernova remnants', *Physical Review D* **105**(8).

Abbott, R., *et al.* (LVK Collaboration) (2022*n*), 'Searches for Gravitational Waves from Known Pulsars at Two Harmonics in the Second and Third LIGO-Virgo Observing Runs', *Astrophysical Journal* **935**(1).

Abbott, R., *et al.* (LVK Collaboration) (2023), 'Open data from the third observing run of ligo, virgo, kagra, and geo', *Astrophysical Journal, Supplement Series* **267**(2).

Acernese, F., *et al.* (LVK Collaboration) (2021), 'Search for Lensing Signatures in the Gravitational-Wave Observations from the First Half of LIGO-Virgo's Third Observing Run', *The Astrophysical Journal* **923**(1), 1401–1424.

Acernese, F., *et al.* (LVK Collaboration) (2022*a*), 'Calibration of advanced Virgo and reconstruction of the detector strain h(t) during the observing run O3', *Classical and Quantum Gravity* **39**(4).

Acernese, F., *et al.* (LVK Collaboration) (2022*b*), 'Search for Gravitational Waves Associated with Gamma-Ray Bursts Detected by Fermi and Swift during the LIGO-Virgo Run O3b', *The Astrophysical Journal* **928**(2), 18601–18620.

Acernese, F., *et al.* (LVK Collaboration) (2022*c*), 'The Virgo O3 run and the impact of the environment', *Classical and Quantum Gravity* **39**(23).

Acernese, F., *et al.* (LVK Collaboration) (2023), 'The Advanced Virgo+ status', *Journal of Physics: Conference Series* **2429**(1), 01203901–01203912.

Acernese, F. *et al.* (VIRGO Collaboration) (2020), 'Quantum backaction on kg-scale mirrors: observation of radiation pressure noise in the advanced virgo detector', **125**(13), 131101.

Acernese, F., *et al.* (VIRGO Collaboration) (2023), 'Virgo detector characterization and data quality: Tools', *Classical and Quantum Gravity* **40**(18).

Calloni, E., *et al.* (LVK Collaboration) (2021), 'High-bandwidth beam balance for vacuum-weight experiment and Newtonian noise subtraction', *European Physical Journal Plus* **136**(3).

Durante, O., Di Giorgio, C., Granata, V., Neilson, J., Fittipaldi, R., Vecchione, A., Carapella, G., Chiadini, F., DeSalvo, R., Dinelli, F. et al.

(2021), ‘Emergence and evolution of crystallization in tio2 thin films: A structural and morphological study’, *Nanomaterials* **11**(6), 1409.

Durante, O., Granata, V., Neilson, J., Carapella, G., Chiadini, F., DeSalvo, R., De Simone, R., Fiumara, V., Pierro, V., Pinto, I. et al. (2023), ‘Investigation of crystallization in nanolayered tio2-based superlattices’, *Surfaces and Interfaces* **41**.

Pierro, V., Fiumara, V., Chiadini, F., Granata, V., Durante, O., Neilson, J., Di Giorgio, C., Fittipaldi, R., Carapella, G., Bobba, F. et al. (2021), ‘Ternary quarter wavelength coatings for gravitational wave detector mirrors: Design optimization via exhaustive search’, *Physical Review Research* **3**(2), 023172.

Uni Sannio/Salerno Group Nanolayering DCC/TDS Documentation

P2100180-v4/ VIR-0076A-22 Improving the precision of e-beam evaporation for nanolayered coatings (23.11.2021).

G2001499-v1/VIR-0040A-22 Nanolayered SIlica/Alumina Composites (14.09.2020).

G2000413-v1/VIR-0040A-22 Which Nanolayers are Worth a Try/Results from UniSannio-UniSa on Nanolayered, prototypes/Stacked Triplet Coatings (16.03.2020).

G1902307-v1/ VIR-0727A-21 Nanolayers Re-Thought (09.12.2019).

G1900356-v3/ VIR-0732A-21 Annealing effect on the nano-meter scale Titania/Silica multi-layers for mirror coatings of the laser interferometer gravitational waves detector (21.06.2019).

G1801365-v3/ VIR-0077A-22 Development of Nanolayered Coatings for the Next Generation of Gravitational Wave Detectors (08.07.2018).

Binary Optimization DCC/TDS Documentation

P2000457-v1/ VIR-0721A-21 On the performance limits of coatings for gravitational wave detectors made of alternating layers of two materials (30.10.2020).

Conferences

O. Durante, "Emergence and Evolution of Crystallization in TiO_2 Thin Films", 108° Congresso Nazionale SIF - 12-16 September 2022, Milano.

V. Granata, "Deposition and characterization of nanolayers for optical metrology", Journées de la Matière Condensée (JMC), 24-27 August 2022, Lyon (France).

Workshop

V.Granata, "Studying the quality of Nanolayered TiO_2/SiO_2 by X ray reflectivity (XRR)", Virgo Week Coating Workshop, 19.04.2021, Online.

V. Granata, "Labs status update and planning Salerno-Sannio Group", Virgo Week Coating Workshop, 11.11.2023, Cascina (Pisa).

V. Granata, "Nanolayers for optical coating", Virgo Week Coating Workshop, 26.01.2023, Cascina (Pisa).

V. Granata, "QDPI @ Salerno/Sannio", Virgo Week Coating Workshop, 07.07.2023, Cascina (Pisa).

V. Granata, "QDPI: A new facility at Sannio/Salerno RU", 2nd Einstein Telescope Annual Meeting, 15.11.2023, Paris-Orsey.

R. De Simone, "Characterization Of Nanostratified Multilayer Structures By Means Of Reflectometric Measurements", Virgo Week Coating Workshop, 10.11.2023, Online.